ProstAtlas: A digital morphologic atlas of the prostate

N. Betrouni [a,b,*], A. Iancu [a,b,c], P. Puech [a,b,c], S. Mordon [a,b], N. Makni [a]

[a] Inserm, U703, 152, rue du Docteur Yersin, 59120 Loos, France
[b] Université Lille - Nord de France, Loos, France
[c] Radiology Departement, Hopital Claude Huriez, CHRU Lille, France

ARTICLE INFO

ABSTRACT

Computer-aided medical interventions and medical robotics for prostate cancer have known an increasing interest and research activity. However before the routine deployment of these procedures in clinical practice becomes a reality, *in vivo* and *in silico* validations must be undertaken. In this study, we developed a digital morphologic atlas of the prostate. We were interested by the gland, the peripheral zone and the central gland. Starting from an image base collected from 30 selected patients, a mean shape and most important deformations for each structure were deduced using principal component analysis. The usefulness of this atlas was highlighted in two applications: image simulation and physical phantom design.

1. Introduction

Prostate cancer (PCa) remains the most commonly occurring malignancy among men in the developed countries. For its support, many researches are undertaken in different aspects including diagnosis, prognostication, and treatment. Thereby, many procedures were developed to assist the clinician. For instance, the diagnosis has experienced an important development through the combination of prostatic specific antigen (PSA), digital rectal examination (DRE) and image-guided biopsy by transrectal ultrasound (TRUS) or magnetic resonance imaging (MRI). For the treatment, in addition to conventional techniques: prostatectomy, radiotherapy and brachytherapy a concept of focal therapies is emerging where the aim is to treat only the tumor. These focal therapies constitute an intermediate option between watchful waiting and radical therapy for small volume and low-grade prostate cancer.

In all these procedures, imaging takes an increasingly growing position and image analysis has become crucial. Starting from this observation and from the ubiquitous need for 3D data set with well-known ground truth to validate image processing tools/algorithms/methods, our motivation was to create a digital morphologic phantom of the prostate and its components. Such solutions was already proposed for brain [1]. The phantom combines a model and MR imaging simulator and is publicly available (www.bic.mni.mcgill.ca/brainweb). A statistical atlas of prostate cancer distribution had been proposed by Shen et al. [2] for optimizing biopsies. It is also free and can be retrieved from the authors' website (www.rad.upenn.edu/sbia/projects/prostate.html).

From a morphologic point of view, the prostate is an exocrine gland, shaped like a pyramid with an upward base. The zonal anatomy of the prostate has been described for the first time in the 60s, but the use of terms in anatomical practice was introduced in the 80s [3]. It is composed of four zones: peripheral zone (PZ), central zone, transition zone (TZ) and fibro-muscular structure (Fig. 1). PZ and TZ are key structures, as 70% of prostate tumors are located within PZ. Inversely, benign hypertrophy (BPH) most often occurs in the transition zone, which becomes larger with age.

From a radiologic point of view, for men aged over 50 years, only two areas of the prostate are considered: the central gland (hypertrophied transition zone and peri-urethral glands) and peripheral zone. In this study, we assume that transition zone (TZ) refers to the central zone. As shown by Fig. 1, TZ is surrounded by the PZ, which thickness and size depend on patient's age and prostate pathological symptoms, like benign hypertrophy (BPH). The PZ is surrounded by vessels and is very likely to host irregular tissues like tumors.

In the next sections, we describe the data and the models used to create the numerical phantom of the gland, the peripheral zone and the transition zone.

2. Materials and methods

2.1. Data

The median age of prostate cancer diagnosis is 74 years, with nearly 66% of cases diagnosed after the age of 70. Before 50 the percentage is about 0.3% [4]. Exams consist of prostate specific

* Corresponding author at: INSERM U703, Institut HIPPOCRATE, 152, rue du Docteur Yersin, 59120 Loos, France. Tel.: +33 320446722.
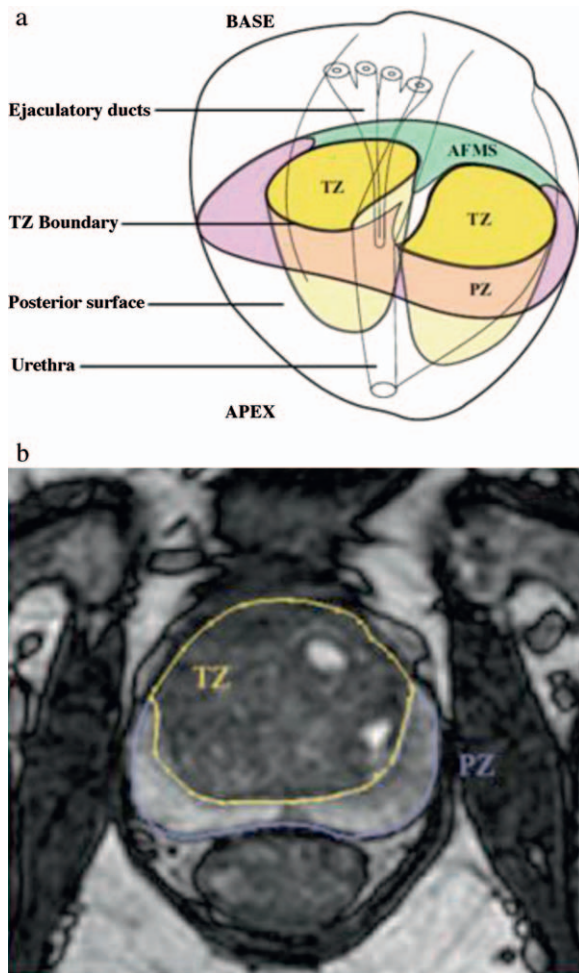E-mail address: n-betrouni@chru-lille.fr (N. Betrouni).

Fig. 1. anatomic description (a) and T2-weighted MRI (b) of an average 60 cc prostate showing its zonal anatomy with a transverse section at the verumontanum level (TZ: transition zone, PZ: peripheral zone, AFMS: anterior fibromuscular stroma).

Table 1
Summary of the characteristic of the selected patients.

Patient	Age (years)	Volumetry (cm³)		Biopsy results	PSA (ng/ml)
		Ultrasound	MRI		
1	55	40	45	Normal	3.93
2	53	54	52	Gleason 7	15.58
3	68	56	58	Gleason 9	3.92
4	72	85	86	Normal	9.7
5	49	35	30	Gleason 6	5.54
6	60	42	41	Gleason 6	5.5
7	65	100	88	Normal	4.7
8	74	90	90	Normal	8.5
9	73	172	170	Normal	4.89
10	60	56	52	Normal	7.25
11	66	30	38	Gleason 6	10
12	73	70	72	Normal	9.28
13	77	44	49	Gleason 7	9.9
14	55	32	34	Gleason 7	9.7
15	56	55	37	Normal	6.15
16	68	83	111	Normal	4.89
17	56	65	75	Normal	6.6
18	74	60	61	Gleason 7	6.55
19	70	130	105	Normal	10.9
20	70	36	35	Gleason 7	2.9
21	71	56	70	Gleason 7	16.76
22	60	65	55	Gleason 6	12.1
23	59	45	46	Gleason 9	9.2
24	58	30	25	Gleason 7	10
25	69	45	40	Normal	9.81
26	56	77	81	Normal	7.09
27	73	45	46	Gleason 6	5.58
28	56	50	43	Normal	6.66
29	66	32	37	Gleason 6	54.63
30	68	35	37	Gleason 7	8.91

these 2 issues and to make the data more suitable for analysis and modelling.

2.2.1. Segmentation

The purpose of this step is to extract the structures (gland, PZ and TZ). Many studies were carried out to introduce automatic methods to segment the prostate on MR data [8–11]. However, often these methods fail at the apex and the base of the gland. Therefore, we preferred a manual delineation. An experienced radiologist involved in the diagnosis of prostate cancer used a homemade software to segment the gland, the PZ and the TZ on the multiparametric MR images. The software is able to spatially register the sequences and provides a friendly user interface where these images sequences are matched with transparency to allow the radiologist to check the contours of the structures (Fig. 2).

At the end of this segmentation process, 30 glands, 30 PZ and 30 TZ were obtained. Each structure was represented by a set of 3D points.

2.2.2. Normalisation and correspondence solving

As the training set contains inter-patients data and the modelling process is based on the variation of the positions of points over the set, it is important to align the points in the same way according to a set of axes. Among the 30 patients, a patient with a prostate of 45 cc (mean value) of volume is chosen as reference and the 29 remaining prostates are aligned on this reference. The alignment (rotation, translation and scaling) is achieved using the Iterative Closest Point (ICP) algorithm [12]. The ICP is based on an iterative alignment of the points through the minimization of a distance function. The method alternates pairing, by associating to each point its nearest neighbour in the second set, and calculation of the transformation between the paired points by solving the system:

This first alignment allows a rigid registration of data. A second alignment is required to have an accurate solving of the
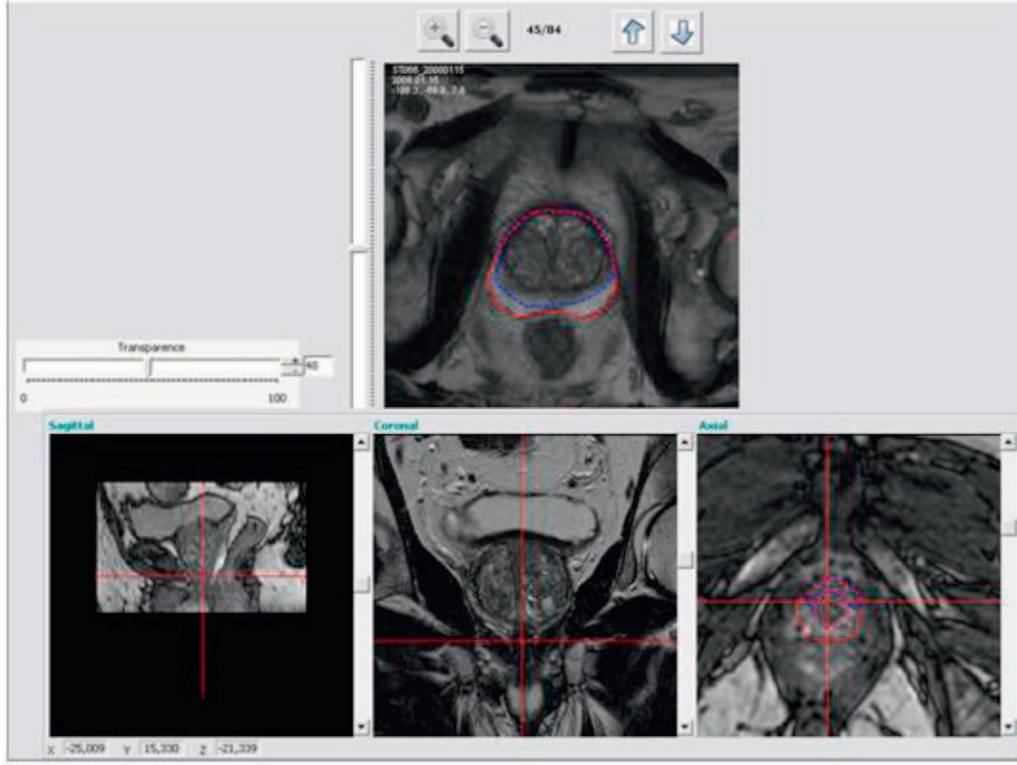
antigen (PSA) measurements coupled with rectal examination for men from 50 to 75.

The normal volume of a young man prostate is 20–30 cc. It was found that 50% of men have prostate benign hypertrophy before 60, this percentage increases to 90% for men of 85 [5]. In a longitudinal study conducted on 1688 men aged from 50 to 75, it was shown that the sole factor influencing the prostate size was the age [6].

Starting from these considerations, an image base was collected. The base contains image from 30 patients, suspected with PCa. Each patient was screened by multi-parametric MRI including an axial 3D T1-weighted BTFE sequence (voxel size 0.48 mm × 0.48 mm × 1.3 mm), an axial T2-weighted sequence (voxel size 0.31 mm × 0.31 mm × 4.0 mm) and a coronal T2 sequence (voxel size 0.31 mm × 0.31 mm × 4 mm). A TRUS guided biopsy was also realized.

Table 1 summarizes characteristics of these patients.

2.2. Preprocessing

In the work of Subsol et al. [7] where the authors presented a global scheme for the construction of morphologic anatomical atlases, they highlighted the fact that building computerized atlases needs to address two majors problems consisting of the definition of shape description parameters and the handling of a large amounts of 3D data. The aim of the preprocessing is to manage

Fig. 2. A user friendly interface used to delineate the structures (the gland, the PZ and the TZ). This interface allows the radiologist to load and to display a multiparametric MR study. Upside image shows a fusion of T2 axial acquisition with an axial 3D BTFE acquisition. Downside images show a 3D navigation between a sagittal BTFE images (reconstructed by MultiPlaner Reconstruction (MPR) of the axial BTFE acquisition), a coronal T2 acquisition and the 3D axial BTFE acquisition. This navigation allows a better delimitation of the apex and the base.

correspondences. It is done by a non-rigid registration. We used the algorithm by Chui and Rangarajan [13]. This method computes the optimal non-rigid mapping between 2 datasets using a local parametric transformation based on Thin Plate Splines (TPS) introduced by Bookstein [14]. The transformation is decomposed into affine and non-affine subspaces. Chui and Rangarajan extended the initial method to simultaneously solve correspondence between points and to determine a thin-plate spline mapping.

2.3. Statistical shape modelling

Starting from these segmented, aligned and normalised data, a model can be generated for each structure (the gland, the peripheral zone and the transition zone). The model is deduced from the training set using Principal Component Analysis (PCA) which enables to extract the mean shape and the most important deformation fields as follows [15].

Model shape of the N ($N = 30$) structures ($X_1 \ldots X_N$), was computed as the mean $\bar{X}$ of the vectors components:

$$\bar{X} = \frac{1}{N} \sum_{i=1}^{N} X_i \tag{1}$$

Main variations around mean shape correspond to eigen values of the covariance matrix S:

$$s = \frac{1}{N-1} \sum_{i=1}^{N} dX_i \overline{dX_1} \tag{2}$$

wherein

$$dX_i = \bar{X} - X_i \tag{3}$$

is the displacement vector.

Each eigen vector is responsible for a variance equal to its eigen value. Its contribution to total shape variation can be expressed as:

$$\alpha_k = \frac{\lambda_k}{\sum \lambda_i} \tag{4}$$

wherein λ_k and α_k represented eigen values and eigen vectors contribution to shape variance, respectively.

Thus, by considering the matrix $\phi = (\phi_1, \ldots, \phi_m)$ composed by the m eigen vectors corresponding to the m most important eigen values, a structure shape could be expressed as:

$$X = \bar{X} + b \cdot \phi \tag{5}$$

wherein $b_1, \ldots, b_m$ is an R^m vector corresponding to the weight vectors. By applying limits to the variation of these weights it can be ensured that a generated shape is similar to those contained in the initial training set.

Usually variation fields are defined in the following field:

$$|b_i| \leq \pm 3 \sqrt{\lambda_i} \tag{6}$$

3. Results

For the gland model, 16 deformation modes were retained. They allowed to capture 95% of the deformations. Table 2 shows the contribution each eigen value.

For the transition zone, 17 deformation modes were selected to obtain a global deformations description of 95% (Table 3).

Note that for these convex structures (gland and transition zone), the first eigen value allow to describe a large field of the deformations (about 58%). It was not the case for the transition zone which form is not convex (Table 4). The 6 first most important eigen values allowed to capture only 52% of the deformations.

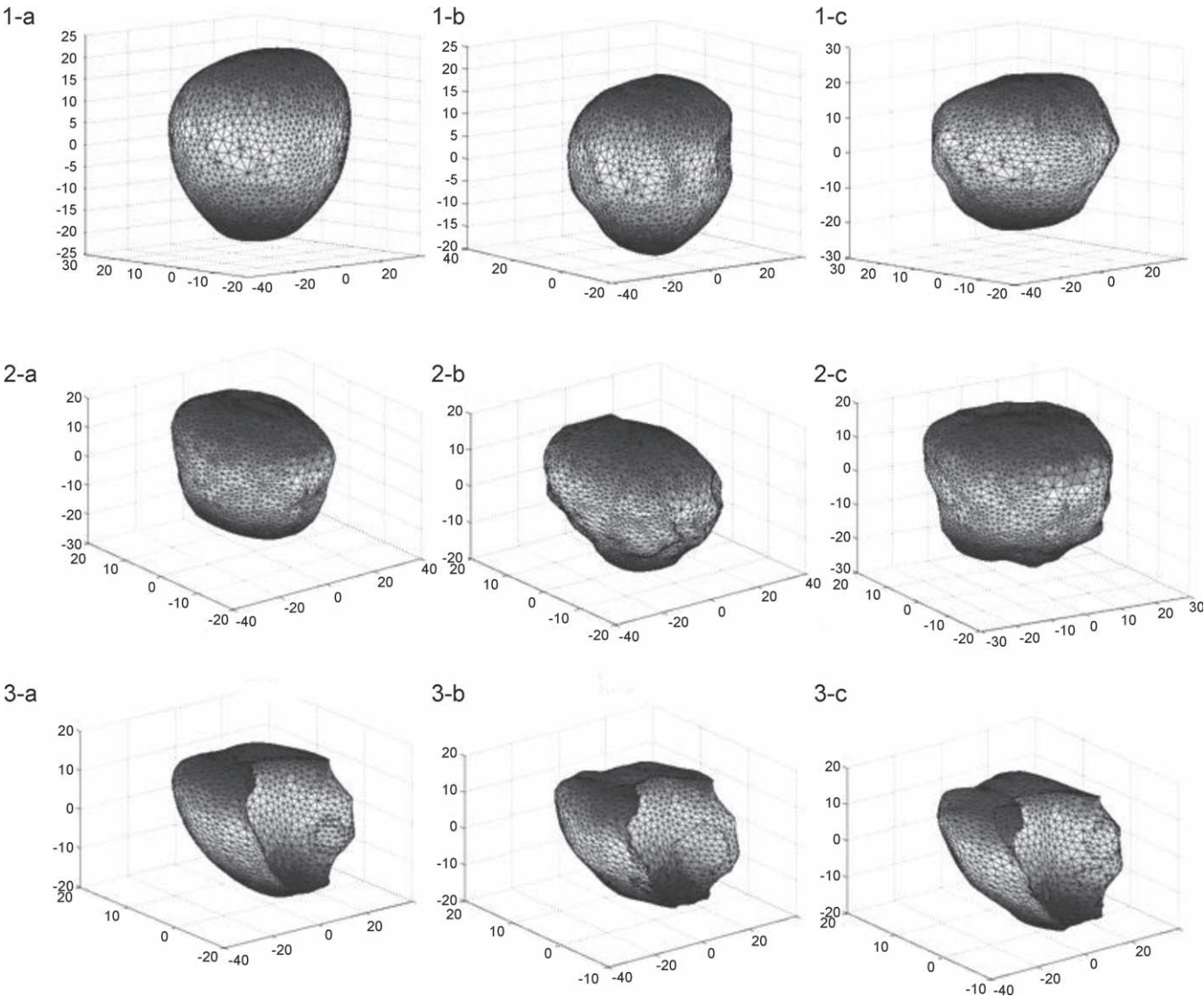Fig. 3 shows some of these deformations for the 3 structures.

Fig. 3. Models and deformations of the structures. Figures 1-a, 1-b and 1-c describe the gland model and 2 deformation modes. Figures 2-a, 2-b and 2-c describe the model and 2 deformations for the transition zone. Figures 3-a, 3-b and 3-c describe the model and 2 deformation mode for the peripheral zone.

Table 2
Individual and coumulative contributions of the 16 eigen values retained to describe the shape variation of the gland.

Eigen value	Individual contribution	Cumulative contribution
1	58.33%	58.33%
2	6.51%	64.84%
3	5.72%	70.56%
4	4.26%	74.81%
5	3.11%	77.82%
6	2.57%	80.50%
7	2.22%	82.72%
8	1.96%	84.68%
9	1.90%	86.58%
10	1.60%	88.18%
11	1.45%	89.62%
12	1.39%	91.02%
13	1.28%	92.30%
14	1.21%	93.51%
15	1.09%	94.60%
16	1.04%	95.65%

Table 3
Individual and cumulative contributions of the 17 eigen values retained to describe the shape variation of the transition zone.

Eigen value	Individual contribution	Cumulative contribution
1	58.58%	58.58%
2	5.91%	64.49%
3	3.88%	68.37%
4	3.34%	71.72%
5	2.77%	74.49%
6	2.50%	76.99%
7	2.32%	79.31%
8	2.24%	81.54%
9	1.96%	83.50%
10	1.89%	85.38%
11	1.78%	87.16%
12	1.63%	88.80%
13	1.50%	90.29%
14	1.43%	91.72%
15	1.36%	93.08%
16	1.25%	94.33%
17	1.22%	95.54%

Table 4
Individual and cumulative contributions of the 19 eigen values retained to describe the shape variation of the peripheral zone.

Eigen value	Individual contribution	Cumulative contribution
1	16.21%	16.21%
2	9.05%	25.17%
3	8.17%	33.34%
4	7.28%	40.63%
5	5.77%	46.40%
6	5.60%	52.00%
7	4.99%	56.99%
8	4.62%	61.61%
9	4.38%	65.98%
10	4.02%	70.00%
11	3.91%	73.91%
12	3.43%	77.35%
13	3.05%	80.39%
14	2.98%	83.37%
15	2.82%	86.19%
16	2.69%	88.88%
17	2.43%	91.31%
18	2.27%	93.58%
19	2.22%	95.80%

4. Applications of the models

4.1. Image simulation

One of the main applications of these phantoms is the simulation of images with perfectly known Gold Truth for the validation of image processing algorithms. For this purpose, the models are used to create empty structures (gland, ZP and ZT) then tissue intensities are mapped in the following way: TZ was filled with its mean MR value (issued from a specified MR sequence for instance T2-weighted, a Diffusion weighted or Dynamic contrast). The PZ level is then deduced using a pre-determined contrast value, which is computed as:

$$C = \frac{|I_{TZ} - I_{PZ}|}{|I_{TZ} + I_{PZ}|} \tag{7}$$

where I_{TZ} and I_{PZ} are mean MR signals of TZ and PZ.

Gaussian noise, with a chosen standard deviation, is then added. Standard median filter was finally applied to reduce salt–pepper effect and smooth the images (Fig. 4).

This process provides morphologically realistic images of the prostate and its substructures based on a known ground truth.

4.2. Physical phantom construction

Current challenges in prostate cancer treatment concern the development of focal therapies to target only the tumor. These new therapeutics like laser therapy, High Intensities Focused Ultrasound (HIFU) or cryotherapy require preclinical evaluation and simulation to accurately plan the intervention. This planning can be done using physical phantoms. However, existing commercial phantoms are designed to guide biopsies or global treatment as brachytherapies and do not allow precise description of the anatomy. We used the digital phantom to construct a physical phantom. It was composed of 2 parts: (i) a fixed part that contains perineum and rectum, and (ii) a removable part with a prostate. The prostate form was created using a 3D printer system starting from the numerical generated model. Thus, different configurations with different prostate sizes were possible (Fig. 5).

The phantom was evaluated using transrectal ultrasound, MRI and real-time thermometry. Diffusing fibers were inserted into the model to simulate a focal treatment conducted by laser interstitial thermotherapy. Prostate cancer boundaries and laser fiber placement were assessed by transrectal ultrasound sonography.
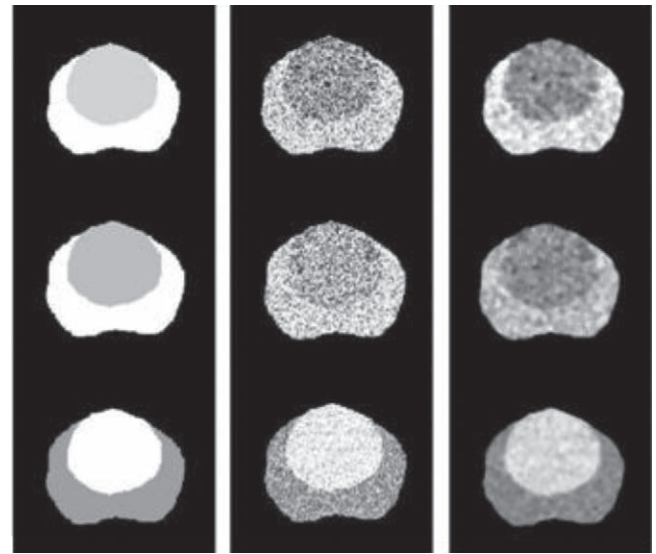

Fig. 4. Image simulation process. From left to right: PZ and TZ labelled with their respective mean level, data with Gaussian noise, data after a smoothing median filter. First, second and third lines represent T2-weighted, T1-CEMRI and DWI, respectively.

These experiments proved that this kind of phantoms allow a real simulation of laser therapy procedure: target definition and fibers placement optimization using MR imaging, treatment delivery and finally treatment monitoring using TRUS imaging.

5. Discussion and conclusion

The benefit of constructing and using digital phantoms is that ground truth becomes available to optimize, control or validate different procedures. In this study we were interested by the creation of a morphologic atlas of the prostate. Indeed, in the last years many computerized and roboterized procedures were developed for prostate cancer management [17–19]. Therefore, it becomes important to have a global framework for validation and comparison of these procedures.

The atlas described in this paper was constructed using data from a selected and representative patients group. We focused the study on the prostate gland and its main parts: the peripheral zone and the transition zone. Principal component analysis allowed to have a description of the main deformations of each structures (Tables 2–4). It allows also to obtain a deformation models to generate e new realistic structures (Fig. 3).

In a previous study we used the same technique to create a prostate model to drive a segmentation process of this organ on MR images [8]. The model was enough for this purpose but as it was created using a limited training data set collected from low resolution images, it does not provide a precise description of the gland morphology especially at the apex and at the base.

The atlas was used in 2 different application, the first concerned image simulation (Fig. 4) where the purpose was to get images of the prostate with a well-known ground truth to validate segmentation algorithms. Besides, the atlas could be combined with the probabilistic tumors atlas proposed by Shen et al. [2]. Consequently, realistic simulation of prostate gland and its structures could be done and tumors distribution mapped to obtain more realistic images to validate detection and staging algorithms.

More sophisticated MR image simulators could be also used to produce more realistic MR images of the phantoms [16].

The second application involves pre-treatment planning. The purpose was the design of a physical realistic phantom to optimize
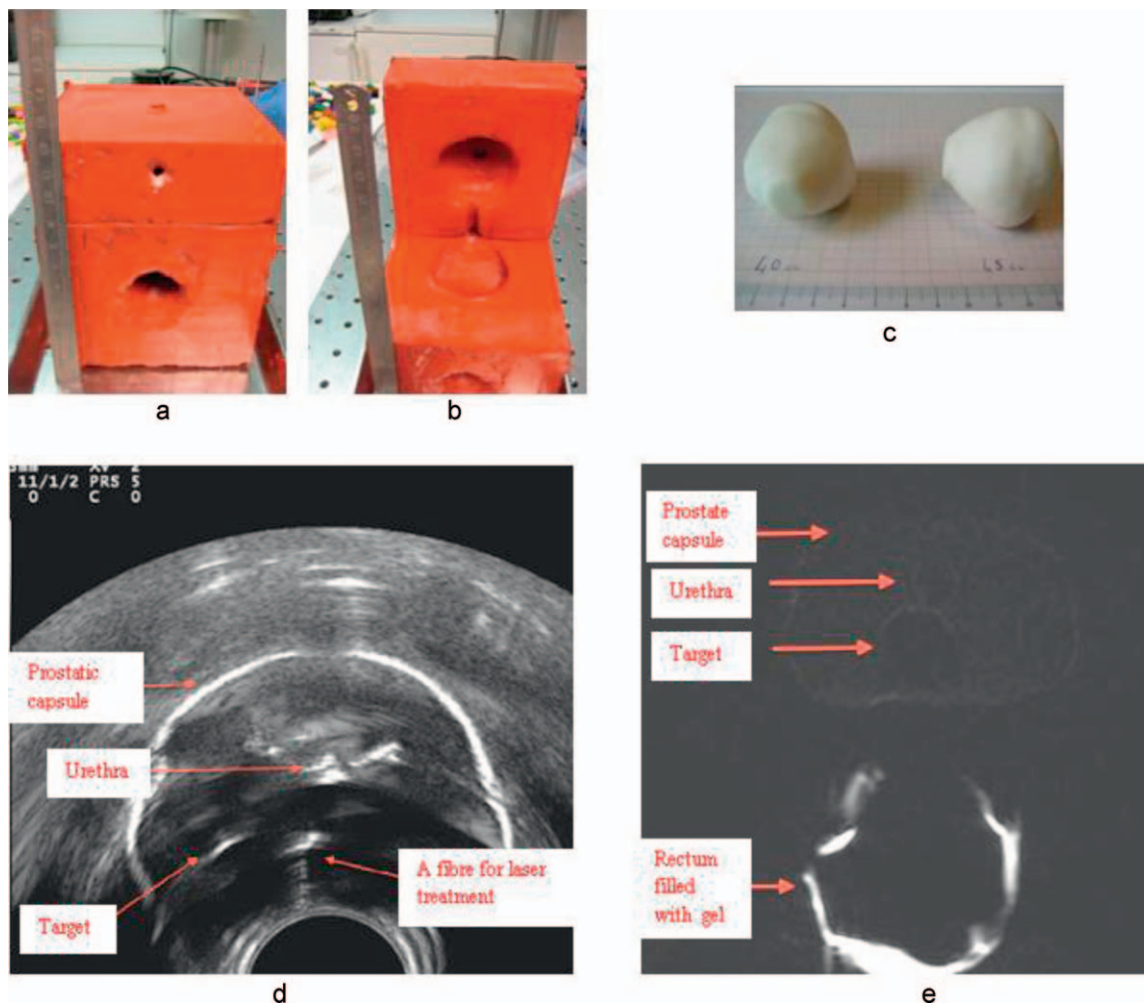
Fig. 5. Physical phantom for focal treatment planning of prostate cancer. (a and b) The phantom with the 2 parts and the prostate emplacement. (c) Two different sizes prostate (40 and 45 cm³) that could be installed in the prostate place inside the phantom. (d) An ultrasound image of the phantom and visualization of the prostate capsule the urethra and a potential target. (e) MR T2 weighted acquisition of the phantom with the visualization of the structures.

a therapeutic approach consisting in introducing laser fiber inside the prostate (the tumor) to perform a focal ablation. Usually this kind of treatment is recommended for low grade prostate cancer for glands from 30 to 60 cm³. Thus, staring from the digital atlas, it was possible to create, using 3D printing technology, different prostates that could inserted in a mold to form a pelvis (Fig. 5). This physical phantom was multimodality compatible and allowed focal targeting.

Similar approach for the construction of an automatically correct physical phantom was described in [20] to test imaging and ablation techniques of prostate cancer. This phantom allowed a good visualisation of the prostate but it was designed to use only a fixed prostate size (80 cm³) and did not permit the modelling of the 2 structures PZ and TZ.

Conflict on interest

The authors declare that there is no conflict on interest.

References

[1] Collins DL, Zijdenbos AP, Kollokian V, Sled JG, Kabani NJ, Holmes CJ, et al. Design and construction of a realistic digital brain phantom. IEEE Trans Med Imaging 1998;17(3):463–8.
[2] Shen D, Lao Z, Zeng J, Zhang W, Sesterhenn IA, Sun L, et al. Optimized prostate biopsy via statistical atlas of cancer spatial distribution. Med Image Anal 2004;8:139–50.
[3] McNeal JE. The zonal anatomy of the prostate. Prostate 1981;2:35–49.
[4] Villers A, Grosclaude P. Epidemiology of prostate cancer. Médecine Nucléaire 2007;32(1):2–4.
[5] Bushman W. Etiology, epidemiology, and natural history of benign prostatic hyperplasia. Urol Clin N Am 2009;36(4):403–15.
[6] Bosch JLHR, Tilling K, Bohnen AM, Bangma CH, Donovan JL. Establishing normal reference ranges for prostate volume change with age in the population-based Krimpen-study: prediction of future prostate volume in individual men. Prostate 2007;67:1816–24.
[7] Subsol G, Thirion JP, Ayache NA. scheme for automatically building three-dimensional morphometric anatomical atlases: application to a skull atlas. Med Image Anal 1998;2(1):37–60.
[8] Pasquier D, Lacornerie T, Vermandel M, Rousseau J, Lartigau E, Betrouni N. Automatic segmentation of pelvic structures from magnetic resonance images for prostate cancer radiotherapy. Int J Oncol Biol Phys 2007;68(2):592–600.
[9] Klein S, van der Heide UA, Lips IM, van Vulpen M, Staring M, Pluim JP. Automatic segmentation of the prostate in 3D MR images by atlas matching using localized mutual information. Med Phys 2008;35(4):1407–17.
[10] Makni N, Puech P, Lopes R, Dewalle AS, Colot O, Betrouni N. Combining a deformable model and a probabilistic framework for an automatic 3D segmentation of prostate on MRI. Int J Comput-assist Radiol Surg 2009;4(2):181–8.
[11] Toth R, Tiwari P, Rosen M, Reed G, Kurhanewicz J, Kalyanpur A, et al. A magnetic resonance spectroscopy driven initialization scheme for active shape model based prostate segmentation. Med Image Anal 2011;5(2):214–25.
[12] Besl PJ, Mckay ND. A method for registration of 3-D shapes. IEEE Trans Pattern Anal Match Intell 1992;14(2):239–56.
[13] Chui H, Rangarajan A. A new algorithm for non rigid point matching. Comput Vis Image Understand 2003;89(2–3):114–41.
[14] Bookstein F. Principal warps: thin-plate splines and the decomposition of deformations. IEEE Trans Pattern Anal Match Intell 1989;11(6):567–85.
[15] Cootes TF, Hill A, Taylor CJ, Haslam J. The use of active shape models for locating structures in medical images. Image Vis Comput 1994;12(6):355–66.

[16] Benoit-Cattin H, Collewet G, Belaroussi B, Saint-Jalmes H, Odet C. The SIMRI project: a versatile and interactive MRI simulator. J Magn Reson 2005;173(1):97–115.

[17] Atalar E, Ménard C. MR-guided interventions for prostate cancer. Magn Reson Imaging Clin N Am 2005;13:491–504.

[18] Troccaz J, Baumann M, Berkelman P, Cinquin P, Daanen V, Leroy A, et al. Medical image computing and computer aided medical interventions applied to soft tissues: work in progress in urology. Proc IEEE 2006;94(9):1665–77.

[19] Zhu Y, Williams S, Zwiggelaar R. Computer technology in detection and staging of prostate carcinoma: a review. Med Image Anal 2006;10:178–99.

[20] Lindner U, Lawrentschuk N, Weersink RA, Raz O, Hlasny E, Sussman MS, et al. Construction and evaluation of an anatomically correct multi-image modality compatible phantom for prostate cancer focal ablation. J Urol 2010;184(1):352–7.